

Exciton condensate in bilayer transition metal dichalcogenides: strong coupling regime

Bishwajit Debnath,¹ Yafis Barlas,² Darshana Wickramaratne,³ Mahesh R. Neupane,⁴ and Roger K. Lake¹

¹*Department of Electrical and Computer Engineering,
University of California, Riverside, CA 92521, USA*

²*Department of Physics and Astronomy, University of California, Riverside, CA 92521, USA*

³*Materials Department, University of California, Santa Barbara, CA 93106, USA*

⁴*Electronics Technology Branch, Sensors and Electron Devices Directorate,
U. S. Army Research Laboratory, Adelphi, MD 20783, USA*

Exciton condensation in an electron-hole bilayer system of monolayer transition metal dichalcogenides is analyzed at three different levels of theory to account for screening and quasiparticle renormalization. The large effective masses of the transition metal dichalcogenides place them in a strong coupling regime. In this regime, mean field (MF) theory with either an unscreened or screened interlayer interaction predicts a room temperature condensate. Interlayer and intralayer interactions renormalize the quasiparticle dispersion, and this effect is included in a *GW* approximation. The renormalization reverses the trends predicted from the unscreened or screened MF theories. In the strong coupling regime, intralayer interactions have a large impact on the magnitude of the order parameter and its functional dependencies on effective mass and carrier density.

I. INTRODUCTION

Electron-hole (e-h) bilayer systems, such as the one illustrated in Fig. 1(a), are good candidates for observing exciton condensation [1]. The presence of an exciton condensate results in a gapped spectrum for the e-h bilayer system, as illustrated in Fig. 1(b). Although there is evidence of exciton condensation in GaAs double quantum wells in the quantum Hall regime [2–5], the zero-field exciton condensate remains elusive. Recently, focus has returned to engineering a bilayer exciton condensate in the absence of a magnetic field in two-dimensional crystals such as graphene and transition metal dichalcogenides [6–13].

Graphene appears to be an attractive candidate for the realization of bilayer exciton condensates due to its perfect particle-hole nesting [6, 7]. Mean field calculations with the bare Coulomb interaction predict high transition temperatures (~ 300 K) [6]. However, screening effects in graphene are of the order of the Fermi wavevector (k_F). As a result, static screening reduces the transition temperatures significantly [8, 11, 14]. The predicted transition temperatures in the e-h graphene bilayer systems range from 1 mK – 100 K [6–8, 11, 15–18], depending on the level of the theory. A study which includes dynamical effects on the screened interactions estimates a transition temperature $T_c \sim 4$ K [19]. Another study taking into account the screening resulting from proximity gates found transition temperatures in the 1 mK–1 K range [11]. Replacing each monolayer of graphene with a bilayer of graphene has been suggested for increasing the transition temperature [20].

The strength of the exciton condensate is proportional to the coupling strength λ , which is the ratio of the interaction energy to the band energy. This ratio is the fine structure constant in graphene given by $\lambda = e^2/[\kappa\hbar v_F] \sim 2.2/\kappa$ [6, 19, 21], where κ is the dielectric constant of the

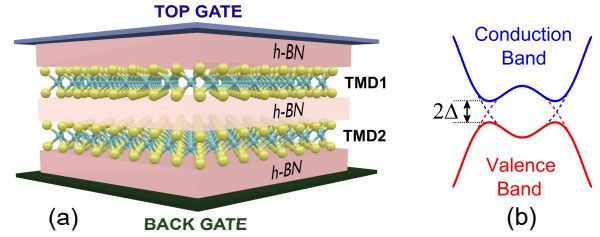


FIG. 1. (a) Illustration of two monolayers of transition metal dichalcogenides separated by a thin film of hexagonal boron nitride (h-BN). The Fermi levels of the top and bottom monolayers are tuned to induce equal electron and hole carrier densities. (b) The conduction band of the electron layer and the valence band of the hole layer overlap, and in the presence of a condensate, a gap (2Δ) opens in the dispersion.

barrier material and v_F is the Fermi velocity. Graphene’s fine structure constant is density independent and typically $\lambda \lesssim 1$, which is a good approximation for weak coupling theories. However for parabolic bands, such as those in bilayer graphene and transition metal dichalcogenides (TMDs), λ is density dependent. In this case, $\lambda \approx 6gm_+/(\kappa k_F)$, where m_+ is the reduced electron-hole mass of the e-h bilayer system, g is the degeneracy, and $k_F \propto \sqrt{n_{2D}/g}$ is the Fermi momentum that depends on electron density n_{2D} . In bilayer graphene, the low effective mass gives $\lambda = 0.2 \sim 1.1$, so that weak coupling theories also apply.

TMDs have larger effective masses and typically larger values of $\lambda = 2.2 \sim 10.4$, depending on the carrier density of $10^{11} \sim 10^{12} \text{ cm}^{-2}$. Larger masses result in larger excitonic binding energies that would appear more suitable for higher exciton gaps and transition temperatures. Mean field calculations using the unscreened Coulomb interactions do predict room temperature condensation, and they also predict higher condensation temperature

for higher carrier densities (n_{2D}). However, for higher carrier densities, screening effects should be considered. In graphene bilayers, screening incorporated within a random phase approximation (RPA) reduces the interlayer coherence, as one would expect. For TMD bilayers, which lie in the strong coupling regime, RPA screening has little effect on the interlayer coherence.

Screening not only affects the *interlayer* interaction, but it also affects the *intralayer* interaction within the same monolayer. The intralayer interaction renormalizes the effective mass and the corresponding λ . We formulate an intermediate/strong coupling theory by incorporating both the interlayer and the intralayer RPA screened interaction into a self-energy correction that renormalizes both the effective masses and the excitonic gaps. The inclusion of the self-energy renormalization reverses the trends predicted from the unscreened and screened MF theories. In the weak coupling limit, the intermediate/strong coupling theory converges to the MF theory with an unscreened interaction.

The remainder of the paper is organized as follows. Section II describes the effective model for TMDs used in this paper. Section III discusses the standard mean field treatment of the model Hamiltonian for the bilayer TMD system with an unscreened interaction. In section IV, we include RPA screening and a self-energy renormalization in a *GW* approximation and compare the predictions of the different levels of theory. Section V summarizes and concludes.

II. EFFECTIVE MODEL FOR E-H TMDS BILAYERS

We consider several TMD electron-hole bilayers separated by an insulating h-BN spacer layer, as illustrated in Fig 1(a). Separation of the electron and hole layers by a barrier reduces the overlap of their respective wavefunctions which reduces the interlayer tunneling and recombination. The Fermi level lies in the conduction band of the top monolayer and in the valence band of the bottom monolayer.

The two layers of the bilayer system can consist of the same TMDs (homo-bilayer) or different TMDs (hetero-bilayer). To achieve high critical temperatures for exciton condensation particle-hole nesting is beneficial, (*i.e.*, $|m_e| = |m_h|$). The electron and hole masses in TMDs are similar but not equal, therefore, we consider different homo- and hetero-layer TMD combinations.

Table I shows the spin-resolved band parameters, the effective masses and maximum 2D carrier density for several monolayer TMDs, calculated using spin-resolved density functional theory [24]. All the *ab initio* calculations, including the geometric relaxation and the electronic band properties, are performed at the hybrid Heyd-Scuseria-Ernzerhof (HSE) level of theory [25] with

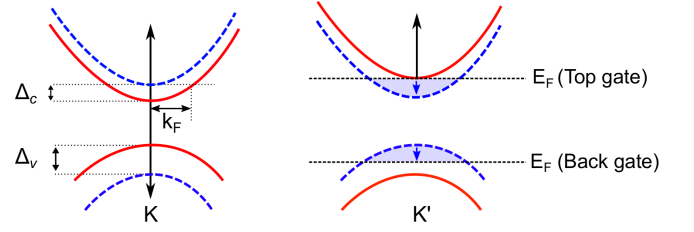


FIG. 2. Spin composition at \mathbf{K} and \mathbf{K}' of monolayer MoX_2 TMDs [23]. Up- and down-spin bands are denoted by solid red and dash-blue lines, respectively. Spin-orbit coupling causes spin splitting of the conduction band (Δ_c) and the valence band (Δ_v).

spin-orbit coupling (SOC). Calculation details are described in Appendix A of [22]. From the effective masses in Table I, we identify several TMD bilayer combinations with partial electron-hole nesting (*i.e.*, $|m_e| \sim |m_h|$). All of the n-type layers are chosen from the MoX_2 materials with spin splitting illustrated in Fig. 2 [23, 26]. The spin splitting of the conduction band Δ_c sets the maximum Fermi level for each calculation. Within this limit, each band of each K-valley is spin polarized.

Treating the electron and hole dispersions as parabolic, the model Hamiltonian for the structure is $\mathcal{H} = \mathcal{H}_0 + \mathcal{H}_{e-e}$,

$$\mathcal{H} = \sum_{\mathbf{k}\sigma\alpha} \epsilon_{\mathbf{k},\sigma}^{\alpha} c_{\mathbf{k}\sigma\alpha}^{\dagger} c_{\mathbf{k}\sigma\alpha} + \frac{1}{2S} \sum_{\mathbf{q}\alpha\beta} v_q^{\alpha\beta} \rho_{\alpha}(\mathbf{q}) \rho_{\beta}(-\mathbf{q}), \quad (1)$$

where $c_{\mathbf{k},\sigma,e}^{\dagger}$ ($c_{\mathbf{k},\sigma,h}^{\dagger}$) denote the electron (hole) creation operators, σ denotes the spin and valley quantum numbers for the electron/hole, $\mathbf{k} = (k_x, k_y)$ is the in-plane two-dimensional momentum with $k = \sqrt{k_x^2 + k_y^2}$, S is the area of the bilayer, $\alpha(\beta) \in \{e, h\}$ are the electron/hole layer indices, $\epsilon_{\mathbf{k},\sigma}^{\alpha=e} = \hbar^2(k^2 - k_F^2)/(2m_{e,\sigma})$, $\epsilon_{\mathbf{k},\sigma}^{\alpha=h} = -\hbar^2(k^2 - k_F^2)/(2m_{h,\sigma})$, k_F is the Fermi momentum, and $m_{e(h),\sigma}$ denotes the spin and valley dependent effective masses for the electron (hole). Time reversal symmetry dictates that $m_{\alpha,\sigma} = m_{\alpha,-\sigma}$. In Eq. (1), $\rho_{\alpha}(\mathbf{q}) = \sum_{\mathbf{k}\sigma} c_{\mathbf{k}+\mathbf{q}\sigma\alpha}^{\dagger} c_{\mathbf{k}\sigma\alpha}$ is the total electron density for the α^{th} layer, $V_{ee} = V_{hh} = 2\pi e^2/(\kappa q)$ is the Fourier transform of the intralayer interaction, and $V_{eh} = V_{he} = -V_{ee}e^{-qd}$ is the Fourier transform of the interlayer interaction, where κ is barrier dielectric constant, d is the thickness of the h-BN insulating spacer, and q is the momentum transfer, $q = |\mathbf{k} - \mathbf{k}'|$.

III. MEAN FIELD THEORY

Mean field decomposition of Eq. (1), gives an effective BCS-like Hamiltonian. The Green's function for the MF

TABLE I. TMD material parameters obtained using density functional theory (HSE-SOC) [22]. m_α is the effective mass at the valence band edge (K_v) and the conduction band edge (K_c), in the units of free electron mass m_0 . κ is the relative dielectric constant. n_{2D} and k_F are the maximum allowed electron density and Fermi wavevector for one-type of spin determined by the conduction spin-splitting energy Δ_c .

Material	Effective Mass (m_α)		Band Splitting		κ	n_{2D} ($\times 10^{12} \text{ cm}^{-2}$)	k_F (nm^{-1})
	Direction	K_v	K_c	$\Delta_v(\text{meV})$	$\Delta_c(\text{meV})$		
MoS ₂	Longitudinal	0.485	0.407	188.6	9.9	3.43	0.4
	Transverse	0.480	0.404				
MoSe ₂	Longitudinal	0.503	0.435	254.8	36.9	4.74	1.7
	Transverse	0.503	0.436				
MoTe ₂	Longitudinal	0.576	0.501	317.4	43.7	5.76	2.3
	Transverse	0.565	0.500				
WS ₂	Longitudinal	0.304	0.331	528.7	12.0	4.13	0.4
	Transverse	0.305	0.332				
WSe ₂	Longitudinal	0.303	0.358	606.4	7.80	4.63	0.3
	Transverse	0.303	0.359				

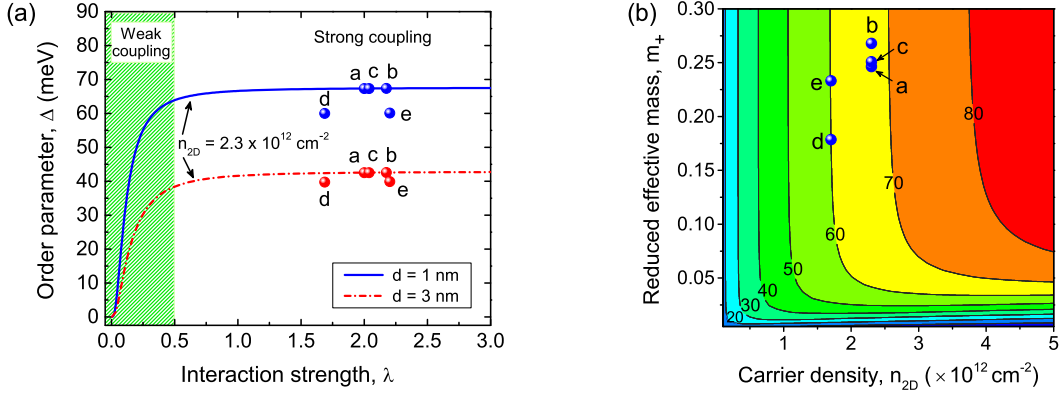


FIG. 3. (a) The order parameter Δ as a function of the interaction strength $\lambda = ge^2m_+/(\pi\kappa\hbar^2k_F)$ for $d = 1.0$ nm (solid line), and $d = 3.0$ nm (dashed line) with $n_{2D} = 2.3 \times 10^{12} \text{ cm}^{-2}$. The spheres give the order parameter for five possible e/h bilayers: a) MoTe₂/MoS₂, b) MoTe₂/MoTe₂, c) MoTe₂/MoSe₂, d) MoSe₂/WSe₂, e) MoSe₂/MoSe₂. In calculating Δ for specific combinations, respective effective masses and the maximum allowed 2D carrier density of the electron layer are used. The interaction strength λ for the TMD bilayers lies in the strong coupling regime. (b) Color contour plot of Δ as a function of m_+ and n_{2D} with $d = 1.0$ nm. The value in meV of each contour is labeled. The positions of the 5 bilayers of (a) are shown.

effective Hamiltonian can be expressed as,

$$\hat{G}_0(k, \omega) = \frac{(\omega - \zeta_k)\hat{\mathcal{I}} + \xi_k\hat{\tau}_3 + \Delta_k\hat{\tau}_1}{(\omega - \zeta_k)^2 - E_k^2 + i\eta}, \quad (2)$$

where $\hat{\tau}_i$ is a Pauli matrix representing the layer pseudospin in the indices α and β ; $\zeta_k = \hbar^2k^2/(4m_{-, \sigma})$, $m_{-, \sigma}^{-1} = (m_{e, \sigma}^{-1} - m_{h, \sigma}^{-1})$, $\xi_k = \hbar^2(k^2 - k_F^2)/(4m_{+, \sigma})$, $m_{+, \sigma}^{-1} = (m_{e, \sigma}^{-1} + m_{h, \sigma}^{-1})$, $E_k = \sqrt{\xi_k^2 + \Delta^2}$, and Δ_k is the order parameter. When $\Delta \rightarrow 0$, the Green function in Eq. (2) reduces to the Green's function of the normal state. The value of the order parameter Δ is evaluated self-consistently,

$$\Delta_{\mathbf{k}} = -\frac{1}{2} \sum_{\mathbf{k}'} V_{eh}(|\mathbf{k} - \mathbf{k}'|) \frac{\Delta_{\mathbf{k}'}}{E_{\mathbf{k}'}}. \quad (3)$$

In general, the order parameter can have a complicated

dependence on momentum, but here we assume a translationally invariant order parameter Δ . We evaluate the normalized order parameter $\bar{\Delta} = \Delta/\epsilon_F$, as a function of the interaction strength λ and the interlayer separation d ,

$$1 = \lambda \int_{-\pi/2}^{\pi/2} d\phi \int_0^{2\cos\phi} d\bar{q} \frac{v_D(q)}{\sqrt{\bar{\xi}_{k-q}^2 + \bar{\Delta}^2}}, \quad (4)$$

where $\bar{\xi}_{k-q} = \xi_{k-q}/\epsilon_F$, $v_D(q) = e^{-k_F q d}$, $\lambda = ge^2m_+/(\pi\kappa\hbar^2k_F)$, κ is the dielectric constant of the h-BN barrier (3.9), g is flavor multiplicity (two-fold for the valley degeneracy), ϕ is the angle between \mathbf{k} and \mathbf{q} , and $\bar{q} = q/k_F$ when $k_F = \sqrt{4\pi n_{2D}/g}$. Note the appearance of the interaction parameter λ , which captures the strength of the interlayer coherence. Eq. (4) is evaluated

self-consistently at $k = k_F$. Henceforth, we restrict our attention to the case where the electron and hole densities are identical, $n_e = n_h = n_{2D}$. We refer to this approach as unscreened mean field (MF) and will denote it as MF.

Figure 3(a) shows the dependence of the order parameter Δ as a function of the coupling parameter λ at a carrier density of $n_{2D} = 2.3 \times 10^{12} \text{ cm}^{-2}$. Eq. (4) predicts that room temperature condensation is possible for $\lambda \gtrsim 0.2$. Due to the exponential dependence of d in Eq. (4), decreasing the interlayer separation from 3 nm to 1 nm increases the order parameter by almost a factor of two.

Figure 3(a) also shows the order parameter Δ for five possible TMD bilayer structures (blue/red spheres): a) MoTe₂/MoS₂, b) MoTe₂/MoTe₂, c) MoTe₂/MoSe₂, d) MoSe₂/WSe₂, e) MoSe₂/MoSe₂. The order parameters for these combinations are calculated using the masses and maximum carrier densities of the n-type layer as listed in Table I. Due to the higher effective masses and lower carrier densities, the values of λ for these bilayer combinations are in the strong coupling regime ($\lambda \sim 2$). Figure 3(b) shows the order parameter Δ in the phase space of the reduced effective mass (m_+) and the electron density (n_{2D}). The positions of the 5 bilayer systems are also shown. As anticipated, the unscreened mean field theory indicates that exciton condensation is favorable for higher 2D carrier densities and larger effective masses.

The unscreened mean field calculations are generally valid for weak coupling regimes ($\lambda \sim 0.5$). Considering that the TMD hetero-structures fall in the strong coupling regime ($\lambda \sim 2$), the theory of exciton condensates in TMDs must be enhanced to include screening and renormalization effects. In the next section, we formulate a strong coupling theory that includes screening of the Coulomb interaction, as well as the effect of quasi-particle renormalization.

IV. INTERMEDIATE/STRONG COUPLING THEORY

In this section, we first include RPA screening and then self-energy renormalization in a *GW* approximation. Results from the different levels of theory are compared.

A. Screened interlayer and intralayer interaction

Screening is treated in the random phase approximation as illustrated in Fig. 4(a). At this level of theory, the solid lines in the polarization diagram represent the Green function of Eq. (2) which includes the coherence term Δ . Δ is calculated from Eq. (4) using the screened interaction self-consistently with the polarization functions.

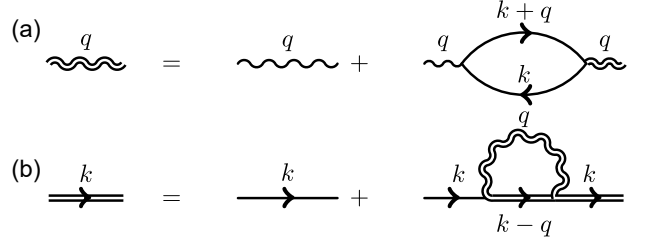


FIG. 4. (a) Screened interaction in the RPA approximation. The Green's function used in the polarization bubble depends on the level of theory. (b) Dyson equation for the Green function in a *GW* approximation that includes both interlayer and intralayer screening.

The polarization is a 2×2 matrix with diagonal terms Π_S corresponding to same-layer polarization, and off-diagonal terms Π_D corresponding to different-layer polarization. When the top and bottom layers have the same carrier density, Π_S and Π_D can be decoupled into even and odd channels, defined as $\Pi_{\pm} = \Pi_S \pm \Pi_D$ where

$$\Pi_{\pm}(q, \omega) = g \int \frac{d^2k}{(2\pi)^2} \left(\frac{E_{k+q} + E_k}{E_{k+q} E_k} \times \frac{E_{k+q} E_k \mp \Delta^2 - \xi_{k+q} \xi_k}{\omega^2 + i\eta - (E_k + E_{k+q})^2} \right). \quad (5)$$

The particle-hole response functions depend on the order parameter Δ and also through the gapped spectrum $E_k = \sqrt{\xi_k^2 + \Delta^2}$, as seen explicitly in Eq. 5. The response function is evaluated self-consistently with the order parameter. From this point onward, we neglect dynamical retardation of the screened interaction and set the frequency $\omega = 0$.

The even polarization function Π_+ captures the density response to the total charge density of the gapped spectrum. Since the total response of a gapped system to a uniform shift in the potential vanishes, $\Pi_+(q \rightarrow 0) = 0$. The odd channel polarization function Π_- captures the response to a difference in the charge density of the two layers. In the $q \rightarrow 0$ limit, the odd channel polarization function approaches the density of states, $\Pi_-(q \rightarrow 0, \omega = 0) = -N(\epsilon_F)$, independent of the gap Δ .

The intralayer and interlayer density response functions needed for the calculations are $\Pi_S = (\Pi_+ + \Pi_-)/2$ and $\Pi_D = (\Pi_+ - \Pi_-)/2$ given by

$$\Pi_S(q) = g \int \frac{d^2k}{(2\pi)^2} \left(1 - \frac{\xi_{k+q} \xi_k}{E_{k+q} E_k} \right) \times \frac{-2E_k}{(E_k + E_{k+q})^2}, \quad (6)$$

$$\Pi_D(q) = g \int \frac{d^2k}{(2\pi)^2} \frac{2\Delta^2}{E_{k+q} (E_k + E_{k+q})^2}. \quad (7)$$

The response functions are normalized to the 2D density of states as $\Pi_{S(D)}(q) = -N(\epsilon_F) \chi_{S(D)}(q)$, where $N(\epsilon_F) = g m_+ / (2\pi \hbar^2)$ is the density of states for the

parabolic bands and $\chi_{S(D)}(q)$ are the dimensionless polarization functions.

The interlayer screened interaction $V_{eh}^{sc}(q)$, within the RPA, can be expressed as $V_{eh}^{sc}(q) = 2\pi e^2/(\kappa q) \cdot v_D^{sc}(\bar{q})$, where

$$v_D^{sc}(\bar{q}) = \frac{\bar{q} [v_D + \tilde{\lambda} (v_S^2 - v_D^2) \chi_D]}{1 - 2\tilde{\lambda}(v_S \chi_S + v_D \chi_D) + \tilde{\lambda}^2 (v_S^2 - v_D^2)(\chi_S^2 - \chi_D^2)}. \quad (8)$$

Here, we define $v_S = 1/\bar{q}$, $v_D = e^{-k_F \bar{q} d}/\bar{q}$ and $\tilde{\lambda} = 2\pi\lambda$. In the limit of an unscreened potential, $v_D^{sc}(\bar{q})$ reduces to $v_D(q) = e^{-k_F \bar{q} d}$ of Eq. (4).

One can now include self-consistent screening in the calculation of the order parameter by replacing the bare Coulomb potential $v_D(q)$ in Eq. (4) with the screened interlayer interaction $v_D^{sc}(q)$, and calculate Δ in Eq. (4), Π_S in Eq. (6), Π_D in Eq. (7), and $v_D^{sc}(q)$ in Eq. (8) self-consistently. We refer to this approach as mean field with RPA screening (MF-RPA).

Electron-electron interactions not only result in screening, but they also renormalize the quasiparticle dispersion. The self-energy renormalization is affected by both the interlayer and the intralayer interactions. Similar to the screened interlayer interaction in Eq. (8), the screened intralayer interactions are $V_{ee}^{sc}(q) = V_{hh}^{sc}(q) = 2\pi e^2/(\kappa q) \cdot v_S^{sc}(\bar{q})$, where

$$v_S^{sc}(\bar{q}) = \frac{\bar{q} [v_S - \tilde{\lambda} (v_S^2 - v_D^2) \chi_S]}{1 - 2\tilde{\lambda}(v_S \chi_S + v_D \chi_D) + \tilde{\lambda}^2 (v_S^2 - v_D^2)(\chi_S^2 - \chi_D^2)}. \quad (9)$$

This correctly reduces to the monolayer RPA interaction in the limit $d \rightarrow \infty$.

The order parameter is directly proportional to the interlayer screened potential v_D^{sc} . The intralayer interaction v_S^{sc} enters into the diagonal element of the self-energy which renormalizes the quasiparticle dispersion (ξ_k) and the interaction strength λ . To understand these effects, we determine the self-energy of Fig. 4(b) and use it to calculate the order parameter self-consistently.

B. Self-energy correction to many-body interaction

The renormalization of both the quasiparticle dispersion and the interlayer interaction are included within a *GW* approximation. The self-energy illustrated in Fig. 5 is calculated self-consistently with the Green's function. The Green's functions used in the polarization diagram include the renormalized order parameter but ignore the mass renormalization. Only the real part of the self-energy is used in the calculation of the Green's function. We refer to this approach as mean field with *GW* renormalization (MF-GW).

Denoting the 2×2 self-energy matrix as $\hat{\Sigma}_c$, the full Green function matrix $\hat{\mathcal{G}}(k, \omega)$ is given by $\hat{\mathcal{G}}^{-1}(k, \omega) = \hat{G}^{-1}(k, \omega) - \hat{\Sigma}_c(k, \omega)$, where \hat{G} is the bare Green function

in Eq. (2). Hence, the full Green function is

$$\hat{\mathcal{G}}^{-1} = \begin{bmatrix} \omega + i\eta - [\xi_k + \mathcal{R}(\Sigma_S)] & -\Delta_0 - \mathcal{R}(\Sigma_D) \\ -\Delta_0 - \mathcal{R}(\Sigma_D) & \omega + i\eta + [\xi_k + \mathcal{R}(\Sigma_S)] \end{bmatrix}, \quad (10)$$

where Δ_0 is the gap function in the absence of the self-energy correction, and \mathcal{R} denotes the real part. It is clear from Eq. (10) that the diagonal element Σ_S renormalizes the quasiparticle dispersion as $\xi_k \rightarrow \xi_k + \mathcal{R}(\Sigma_S)$, and the off-diagonal element Σ_D renormalizes the gap function as $\Delta_0 \rightarrow \Delta_0 + \mathcal{R}(\Sigma_D)$.

We calculate the diagonal self-energy as

$$\Sigma_S(k, \omega - \Omega) = i \int \frac{d\Omega}{2\pi} \int \frac{d^2 q}{(2\pi)^2} v_S^{sc}(q) \hat{\mathcal{G}}_S(k - q, \omega - \Omega), \quad (11)$$

where $\hat{\mathcal{G}}_S$ is the diagonal part of the Green's function in Eq. (10). We take the complex path integral over Ω in Eq. (11) and calculate the normalized diagonal self-energy in the static limit ($\omega \rightarrow 0$),

$$\mathcal{R}(\bar{\Sigma}_S(\bar{k})) = - \left(\frac{\lambda}{\pi} \right) \int_0^{2\pi} d\phi \int_0^2 d\bar{q} v_S^{sc}(\bar{q}) \Theta(k_F^2 - |\mathbf{k} - \mathbf{q}|^2) \times \frac{-|\bar{\xi}_{k-\bar{q}}^R|}{\sqrt{[\bar{\xi}_{k-\bar{q}}^R]^2 + \bar{\Delta}^2}}, \quad (12)$$

where $\bar{\xi}_{k-\bar{q}}^R = \bar{k}^2 - 2\bar{q}\bar{k} \cos \phi + \bar{q}^2 - 1 + \mathcal{R}\{\bar{\Sigma}_S(\bar{k} - \bar{q})\}$ takes into account the renormalization of the quasiparticle dispersion. Θ is the unit step function, and $\bar{\Sigma}_S = \Sigma_S/\epsilon_F$. Since $\bar{\Sigma}_S(\bar{k})$ in Eq. (12) requires the evaluation of $\bar{\Sigma}_S(\bar{k} - \bar{q})$, we use analytical continuation properties, *i.e.*, $\mathcal{R}(\bar{\Sigma}_S(\bar{k})) = \mathcal{R}(\bar{\Sigma}_S(-\bar{k}))$. A separate calculation of the off-diagonal self-energy Σ_D is avoided by self-consistently absorbing it in the definition of $\bar{\Delta}$,

$$1 = \lambda \int_{-\pi/2}^{\pi/2} d\phi \int_0^{2 \cos \phi} d\bar{q} \frac{v_D^{sc}(\bar{q})}{\sqrt{[\bar{\xi}_{1-\bar{q}}^R]^2 + \bar{\Delta}^2}}. \quad (13)$$

The value of $\bar{\Delta}$ determined from Eq. (13) is used self-consistently in determining the polarization functions Π_S and Π_D and thus the screened interactions v_D^{sc} and v_S^{sc} . The dispersion represented by ξ_k used in the calculation of the polarization functions is the bare dispersion in the absence of Σ_S . Thus, the Green function lines in the polarization bubble are partially self-consistent in that they include the effect of the self-energy on the off-diagonal order parameter, but they do not include the effect of mass renormalization. Eqs. (6), (7), (8), (9), (12), and (13) are the set of self-consistent equations that are solved to obtain Δ .

To understand the relative contribution of the self-energy correction, we plot the normalized $\mathcal{R}(\Sigma_S)$ in Fig. 5 for different values of λ . In the weak coupling regime

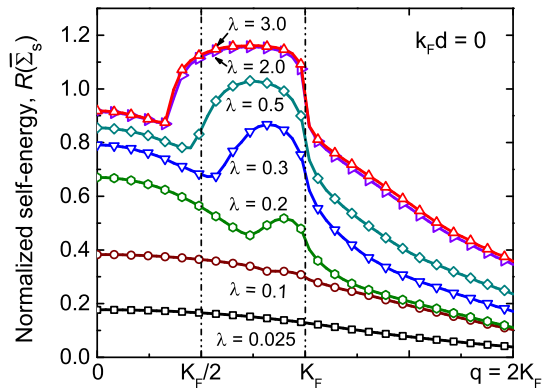


FIG. 5. Real part of the diagonal self-energy $\Sigma_S(q)$ normalized to ϵ_F for $k_F d = 0$.

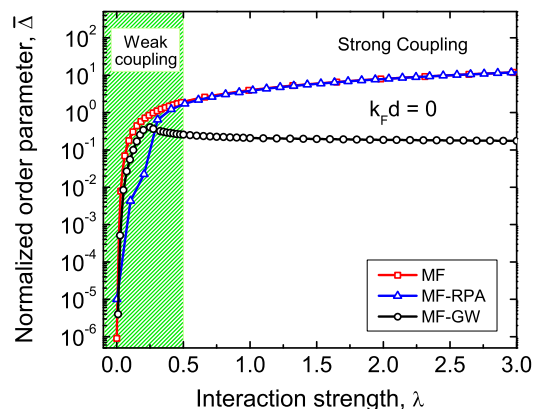


FIG. 6. Normalized order parameter as a function of the effective interaction strength λ , obtained from MF, MF-RPA, and MF-GW theory for $k_F d = 0$.

($\lambda < 0.2$), the self-energy is only 20% – 60% of the Fermi energy. However, at the onset of intermediate/strong coupling region ($\lambda \geq 0.5$), the self-energy becomes equal to or larger than the Fermi energy. This illustrates the importance of the self-energy correction in the strong coupling regime.

C. Discussion

In this section, we discuss the MF-GW results and compare them with the MF and MF-RPA predictions. Theoretically, the most favorable condition of condensation occurs at vanishing interlayer distance, *i.e.* $k_F d \rightarrow 0$. Considering this optimum condition, Fig. 6 summarizes the three different levels of theory. For the MF calculation the gap increases monotonically with interaction strength. In this case, moderate interlayer interaction ($\lambda > 0.2$) leads to room temperature condensation. The effect of RPA screening (MF-RPA) on the order parameter depends on the relative strength of λ . In the

weak coupling regime ($\lambda \approx 0.25$), screening reduces the interlayer coherence. In the intermediate/strong coupling regime, screening cannot compete with the interlayer interaction and Δ follows the unscreened gap function. When both interlayer and intralayer screening are included as a self-energy correction (MF-GW), the interlayer coherence is strongly reduced for interaction strengths above 0.25. As $\lambda \rightarrow 0$, the MF-GW theory and the MF theory coincide. The reason is apparent from Fig. 5, which shows that self-energy correction remains negligible up to $\lambda \sim 0.1$.

Figure 7 is a color contour plot of Δ as a function of m_+ and n_{2D} determined from the MF-GW theory. The positions of the same bilayer structures from Fig. 3 are shown. A comparison of the $m_+ - n_{2D}$ phase diagram in Fig. 7 with that of the MF result in Fig. 3(b) shows that MF-GW theory predicts trends that are qualitatively different from the MF theory. For a reduced mass greater than 0.05, the order parameter of MF theory is nearly independent of the mass and is moderately dependent on the density, changing by a factor of ~ 3 as the density increases an order of magnitude from $5 \times 10^{11} \text{ cm}^{-2}$ to $5 \times 10^{12} \text{ cm}^{-2}$. The order parameter of MF-GW theory has the same moderate dependence on the density, but it is exponentially dependent on the mass. For a density of $2 \times 10^{12} \text{ cm}^{-2}$, the order parameter decreases 5 orders of magnitude as the mass increases from 0.05 to 0.3. Also, the functional dependence of the order parameter on the mass is qualitatively different. In both theories, the order parameter rapidly increases as m_+ increases from zero. In MF theory, the order parameter saturates and remains constant for $m_+ \gtrsim 0.1$. In MF-GW theory, the order parameter peaks at $m_+ \sim 0.025$ and then exponentially decays as m_+ increases. For MF theory, the conditions for maximum Δ occur at the upper right corresponding to high density and high mass. For MF-GW theory, the conditions for maximum Δ occur at the lower left corresponding to low density and low mass. The MF-GW theory exponentially reduces the magnitude of the order parameter for masses corresponding to those of the 2D bilayers. The heavy masses of the 2D materials which increase the order parameter in MF theory, decrease the order parameter in MF-GW theory.

As shown in Fig. 6, *interlayer* screening calculated self-consistently in the presence of a condensate has little effect on the order parameter in the strong coupling limit. Renormalization due to *intralayer* screening has a large effect. We conclude that, in the strong coupling limit, the *intralayer* interactions determine the overall trends of the order parameter.

V. CONCLUSION

Exciton condensation is analyzed as a function of the coupling strength with a focus on the strong coupling

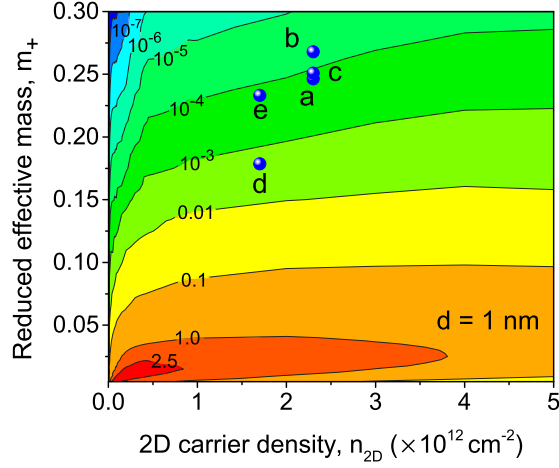


FIG. 7. Color contour plot of Δ as a function of m_+ and n_{2D} with $d = 1.0$ nm calculated with MF-GW theory. The value in meV of each contour is labeled. The positions of the 5 bilayers from Fig. 3(a) are shown.

regime, which is the regime of TMD bilayer electron-hole systems. Three different levels of theory are considered. Starting from unscreened mean field theory, RPA screening and self-energy renormalization in a *GW* approximation are included. A mean field calculation with an unscreened Coulomb potential predicts a room temperature exciton condensate. The inclusion of RPA screening in the interlayer interaction reduces the order parameter in the weak coupling regime, but it has little effect in the strong coupling regime, and a room temperature condensate is still predicted. The inclusion of the effects of both the interlayer and intralayer interactions through a self-energy correction to the quasiparticle dispersion and the order parameter in a *GW* approximation reverses the trends predicted from the MF and MF-RPA theories. The MF-GW theory favors low density and low mass for maximizing the magnitude of the order parameter. The heavy masses of the TMD materials that increase the order parameter in MF and MF-RPA theories, reduce the order parameter in the MF-GW theory. In the strong coupling regime, *intralayer* screening has a large impact on the magnitude of the order parameter and its functional dependencies on effective mass and carrier density.

ACKNOWLEDGEMENTS

This work was supported in part by the National Science Foundation under Award NSF EFRI-1433395 and by FAME, one of six centers of STARnet, a Semiconductor Research Corporation program sponsored by MARCO and DARPA. This work used the Extreme Science and Engineering Discovery Environment (XSEDE),

which is supported by National Science Foundation grant number ACI-1053575.

-
- [1] Y. E. Lozovik and V. Yudson, Zh. Eksp. Teor. Fiz **71**, 738 (1976).
 - [2] L. V. Butov, A. Zrenner, G. Abstreiter, G. Böhm, and G. Weimann, Phys. Rev. Lett. **73**, 304 (1994).
 - [3] I. B. Spielman, J. P. Eisenstein, L. N. Pfeiffer, and K. W. West, Phys. Rev. Lett. **84**, 5808 (2000).
 - [4] M. Kellogg, J. P. Eisenstein, L. N. Pfeiffer, and K. W. West, Phys. Rev. Lett. **93**, 036801 (2004).
 - [5] E. Tutuc, M. Shayegan, and D. A. Huse, Phys. Rev. Lett. **93**, 036802 (2004).
 - [6] H. Min, R. Bistritzer, J.-J. Su, and A. H. MacDonald, Phys. Rev. B **78**, 121401 (2008).
 - [7] C.-H. Zhang and Y. N. Joglekar, Phys. Rev. B **77**, 233405 (2008).
 - [8] M. Y. Kharitonov and K. B. Efetov, Phys. Rev. B **78**, 241401 (2008).
 - [9] A. Perali, D. Neilson, and A. R. Hamilton, Phys. Rev. Lett. **110**, 146803 (2013).
 - [10] D. S. L. Abergel, M. Rodriguez-Vega, E. Rossi, and S. Das Sarma, Phys. Rev. B **88**, 235402 (2013).
 - [11] M. V. Fischetti, Journal of Applied Physics **115**, 163711 (2014).
 - [12] F.-C. Wu, F. Xue, and A. H. MacDonald, Phys. Rev. B **92**, 165121 (2015).
 - [13] J.-J. Su and A. H. MacDonald, Phys. Rev. B **95**, 045416 (2017).
 - [14] R. Gorbachev, A. Geim, M. Katsnelson, K. Novoselov, T. Tudorovskiy, I. Grigorieva, A. MacDonald, S. Morozov, K. Watanabe, T. Taniguchi, *et al.*, Nature Physics **8**, 896 (2012).
 - [15] Y. E. Lozovik and A. A. Sokolik, JETP Letters **87**, 55 (2008).
 - [16] Y. Lozovik and A. Sokolik, Physics Letters A **374**, 326 (2009).
 - [17] E. Y. Lozovik and A. A. Sokolik, The European Physical Journal B **73**, 195 (2010).
 - [18] M. P. Mink, H. T. C. Stoof, R. A. Duine, and A. H. MacDonald, Phys. Rev. B **84**, 155409 (2011).
 - [19] I. Sodemann, D. A. Pesin, and A. H. MacDonald, Phys. Rev. B **85**, 195136 (2012).
 - [20] M. Zarenia, A. Perali, D. Neilson, and F. Peeters, Scientific reports **4**, 7319 (2014).
 - [21] Y. E. Lozovik, S. L. Ogarkov, and A. A. Sokolik, Phys. Rev. B **86**, 045429 (2012).
 - [22] D. Wickramaratne, Ph.D. thesis, University of California Riverside, 2015.
 - [23] A. Kormányos, G. Burkard, M. Gmitra, J. Fabian, V. Zólyomi, N. D. Drummond, and V. Fal'ko, 2D Materials **2**, 022001 (2015).
 - [24] G. Kresse and J. Furthmüller, Computational Materials Science **6**, 15 (1996).
 - [25] J. Heyd, G. E. Scuseria, and M. Ernzerhof, The Journal of Chemical Physics **118**, 8207 (2003).
 - [26] Z. Y. Zhu, Y. C. Cheng, and U. Schwingenschlögl, Phys. Rev. B **84**, 153402 (2011).